MATERIALS CHEMISTRY
FRONTIERS

RESEARCH ARTICLE

View Article Online
View Journal

Cite this: DOI: 10.1039/d5qm00921a

First-principles modelling of circularly polarized luminescence in one-handed helical ladder polymers

Giovanni Bella,* Marco Milone, Giuseppe Bruno and Antonio Santoro

The idea of helical chirality bridges the gap between stereogenic asymmetry at the local scale and intrinsic non-superimposability in larger secondary structures (DNA, RNA, α-helix protein, *etc.*). Novel synthetic breakthroughs allowed the ascent of a brand-new subclass of chiral materials based on defect-free single-handed helical ladder polymers, reducing the conceptual barrier between small artificial helical foldamers and helical biomacromolecules. Beyond their extraordinary physicochemical properties, the interference of circularly polarized radiation with optically pure one-handed helical ladder polymers paved the way for pronounced circularly polarized luminescence events. This work, through a systematic theoretical investigation, tackled the CPL spectral profiles of a multitude of enantiomeric ladder-type polymers with diversified helical arrangements and topological cavities. The computational protocol integrated a preliminary ground state treatment of chiral monomeric units with excited-state molecular dynamics of oligomeric and polymeric systems to understand how key geometrical parameters of ladderization precursors vary upon photoexcitation for chemical architectures of increasing size. The consolidation of APFD and O3LYP functionals performances, through the rigorous assessment of chiroptical descriptors (emission energies, rotational strengths, electric/magnetic transition dipole moments and their angle), allowed us to evaluate how the chiral dimensionality orients the CPL spectra of one-handed helical ladder polymers in terms of peak position, band shape, chiral sign and signal magnitude.

Received 23rd December 2025,
Accepted 10th February 2026

DOI: 10.1039/d5qm00921a

rsc.li/frontiers-materials

1. Introduction

Helicity pervades the universe; our ''genetic code'' is stored inside a microscopic double-helix filament while we are constantly travelling aboard a planet that follows a helical trajectory around the center of the Milky Way galaxy. Although scientists cannot influence helicity at the astronomical level, many chemists have been fascinated by helices and consequently several helix patterns have been intentionally constructed at the molecular scale in recent decades.[1–10] Inspired by the design of macrobiomolecules, synthetic chemists successfully accessed covalent abiotic helically wrapped architectures through the ladderization process[11–14] and chirality-assisted synthesis (CAS).[15–17] Benefiting from these two approaches, the resultant shape-persistent system consists of a non-planar fully π-conjugated backbone in which the ladder-like arrangement is governed by building blocks that regio- and stereo-specifically form two (or more) new bonds with another repeating unit[18–21](Fig. 1). In addition to a variety of programmable properties (superior thermal stability,[22] mechanical properties,[23] high resistance over extreme chemical conditions[24]), this kind of well-defined linkage geometry confers a defect-free molecular identity with intrinsic configurable chirality,[25–28] which is impossible to achieve with typical non-geometrically controlled polymerization[29] or transient chiral-torsioned molecules.[30–33] Specifically, this exceptional chiral designability is promoted by an uninterrupted sequence of adjacent rings (sharing two or more atoms), which permits a predictable one-handed (levorotatory/dextrorotatory) twisting direction.[34] This source of asymmetry, originating from a rigid three-dimensional helical disposition, imparts the whole chemical structure with intriguing chiroptical properties involving both absorptive and emissive mechanisms. In 2019, Ikai *et al.* prepared the first optically active one-handed helical polymer, exploiting enantio-induction into a D_{3h} triptycene core to measure a strong bisignate circular dichroism (CD) signal.[35] In 2021, the appropriate incorporation of a proper luminophore inside the helical pitch allowed Yashima *et al.* to fabricate the first single-handed helical polymer showing intense circularly polarized luminescence (CPL).[26] That

---

Department of Chemical, Biological, Pharmaceutical and Environmental Sciences, University of Messina, Viale F. Stagno d'Alcontres 31, 98166 Messina, Italy. E-mail: gbella@unime.it

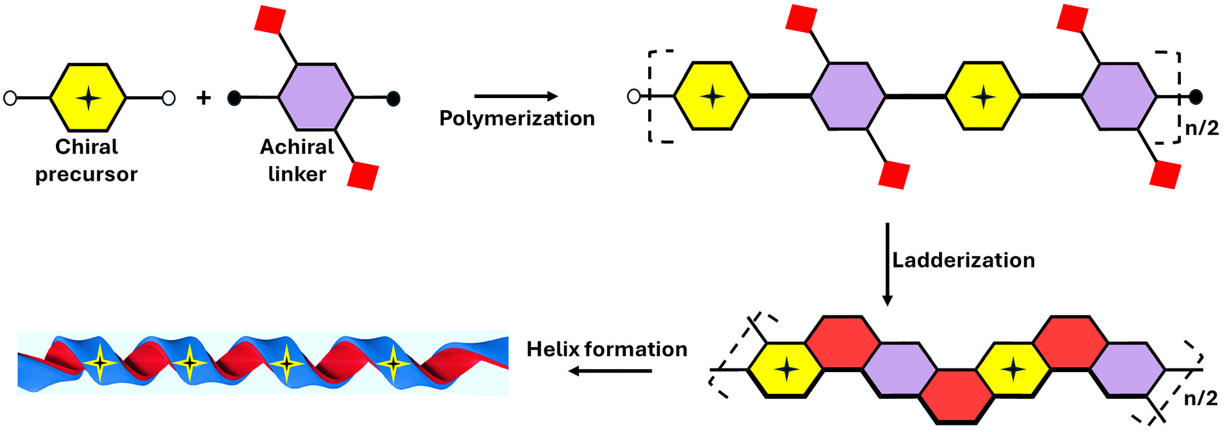

Fig. 1 General stereospecific synthetic sequence to obtain one-handed helical ladder polymers.

pioneering research, based on modulating helical secondary structures, opened the way toward a new generation of CPL-active ribbon-/coil-like polymers. In this less-explored landscape, theoretical modelling is scarce and mainly involves circular dichroism phenomena.[36,37] Notwithstanding the rising enthusiasm for CPL *in silico* predictions,[38–42] to date only one example (a spirobifluorene dimer) of helical ladder CPL simulation has been reported in the literature.[43] With the present contribution, we propose a multilevel computational approach that starts with the chiroptical investigation of monomeric units and evolves toward gradually longer one-handed helical strings, with the goal of decoding how CPL signals vary with chain length. In detail, six different cases (covering the whole literature on this topic) manifesting various ladderization precursors with specific chiral linkages, will be inspected in order to define a density functional theory (DFT) protocol that is able to clarify how helical size dependence dominates chiral emissions in diverse 3D asymmetric contexts. Considering the intimate relationship between structural and chiroptical characteristics in the helical ladder superstructures, a preliminary part of our study is dedicated to finding a reliable level of theory to correctly reproduce the geometrical features of the ground state (S0) of the proposed monomeric and polymeric models. Hence, the central part of the workflow is focused on excited molecular dynamics aimed at mapping the first excited state (S1) of the chiral materials with the objective of understanding how key geometrical parameters change upon photoexcitation. Lastly, time-dependent (TD) DFT formalism was used to critically evaluate which exchange–correlation functionals can be universally applied to decipher the CPL spectral profiles in terms of peak position, band shape and chiral intensity.

2. Results and discussion

First, we focused our theoretical investigation on all six CPL-active examples of one-handed helical ladder polymers reported in the literature,[25–28] deliberately excluding random ladder structures (whose chiral existence was not interpretable) and supramolecularly doped helical ladder assemblies.[20] Bearing in mind that molecular chiroptical identity is strictly connected to the spatial organization of atoms and being conscious that geometrical parameters of monomeric units are chemically transmitted to the entire polymeric building,[44] we decided to execute DFT optimization screening on the polymerization precursors. The location of the extended helical ladder system within the hypersurface of potential energy (PES) will be deeply influenced by the quality of the energy-minimized monomer, which heavily depends on the choice of the exchange–correlation functional. In theoretical analyses, the performance of functionals is commonly benchmarked by comparing the computed atomic positions with the crystallographic coordinates.[45–48] This computational strategy was required because, notwithstanding the exceptional properties of one-handed helical ladder polymers, the degree of crystallinity was not high enough to collect single-crystal X-ray diffraction (SC-XRD) data for the entire molecular ribbon. Fig. 2 shows the X-ray characterized monomeric scaffolds used to engineer their respective helical ladder polymers (the fifth and sixth helical ladders were generated by constitutional isomers of monomers 4 and 3, respectively, Fig. S1, SI). Temporarily neglecting the possible helicization peculiarities in the macromolecular coils, to emulate the geometrical conformations of the relative monomeric constituents, an exhaustive set of DFT functionals was interrogated. For this task, functionals already adopted for DFT optimizations of helical ladder fragments[19,25,27,28] and for carbon-based materials[49–55] were tested. Therefore, B3LYP, CAM-B3LYP, TPSSTPSS, BLYP, B97D3, ωB97xD, mPW1PW91, MN12L, PW6B95D3 and LC-ωHPBE were checked in the gas phase for direct matching with the crystallographic atomic positions. Consistent with previous papers, the Pople basis set was combined with the above functionals, due to its ability to model second-period atoms.[56,57]

The structural root-mean-square deviations (RMSD) illustrated in Table 1 evidence comparable performances among the various functionals for each building block without excessive fluctuations. The high RMSD values can be ascribed to the

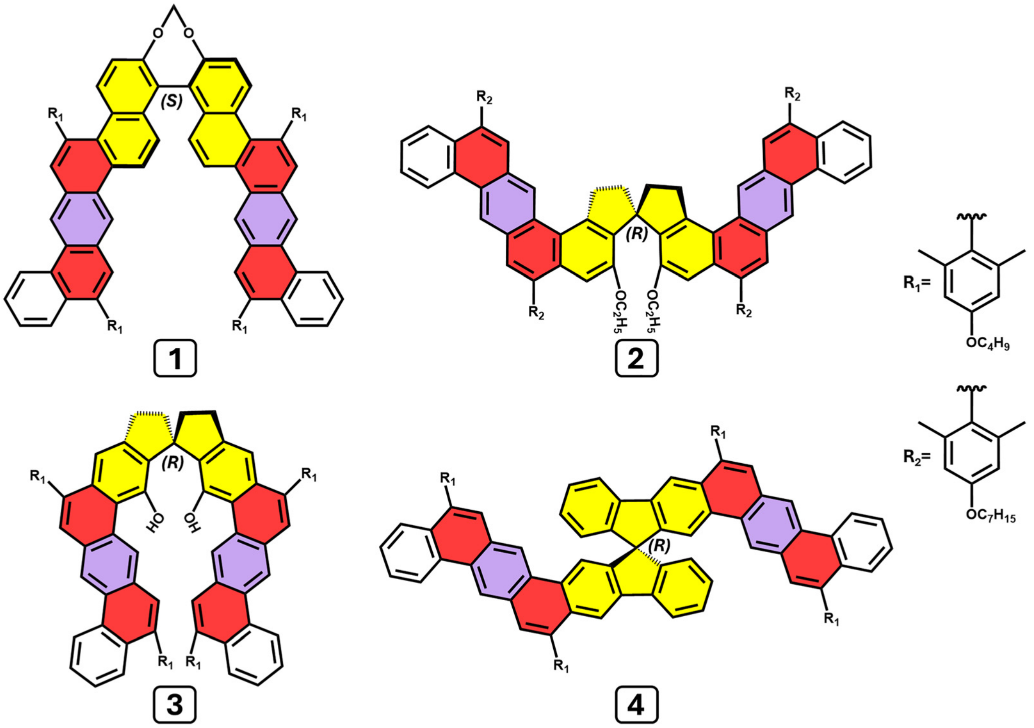

Fig. 2 Structures of the monomeric units based on X-ray crystallographic data; colour labelling is consistent with Fig. 1.

Table 1 Comparison of the exchange–correlation functionals (coupled with 6-311G(d,p) basis set in gas phase) as assessed by RMSD, RMSD of truncated forms () and dihedral angle φ []. Digits in bold style refer to dihedral angle deltas

	RMSD/φ			
Functional	1	2	3	4
B3LYP	2.879 (2.215) [55.003] 3.514	1.424 (0.653) [43.391] 2.977	1.788 (1.397) [44.205] 3.618	0.697 (0.607) [57.839] 6.080
CAM-B3LYP	2.856 (2.202) [55.354] 3.163	1.324 (0.601) [42.174] 1.760	1.728 (1.380) [44.259] 3.564	0.694 (0.598) [57.890] 6.029
TPSSTPSS	2.888 (2.211) [53.852] 4.665	1.386 (0.643) [43.414] 3.000	1.800 (1.398) [44.193] 3.630	0.699 (0.603) [57.877] 6.042
BLYP	2.946 (2.266) [54.667] 3.850	1.494 (0.692) [44.114] 3.700	1.798 (1.397) [43.302] 4.521	0.697 (0.616) [57.846] 6.073
B97D3	3.006 (2.352) [51.923] 6.594	1.438 (0.617) [37.293] 3.121	1.812 (1.442) [43.155] 4.668	0.808 (0.721) [57.048] 6.871
ωB97xD	2.951 (2.297) [53.843] 4.674	1.460 (0.710) [37.142] 3.272	1.757 (1.424) [42.851] 4.972	0.735 (0.658) [57.745] 6.174
mPW1PW91	2.881 (2.244) [54.649] 3.868	1.385 (0.658) [43.026] 2.612	1.744 (1.472) [44.104] 3.719	0.703 (0.606) [57.012] 6.907
MN12L	3.082 (2.419) [52.873] 5.644	1.431 (0.812) [34.668] 5.746	1.775 (1.444) [42.081] 5.742	0.770 (0.658) [57.788] 6.131
PW6B95D3	3.111 (2.432) [53.112] 5.405	1.458 (0.655) [36.074] 4.340	1.973 (1.566) [41.853] 6.240	0.719 (0.650) [57.724] 6.195
LC-ωHPBE	2.865 (2.234) [55.144] 3.373	1.364 (0.619) [42.191] 1.777	1.735 (1.435) [44.231] 3.592	0.701 (0.616) [57.857] 6.062
X-ray	[58.517]	[40.414]	[47.823]	[63.919]

flexible relaxations of the alkyl chains, which may differ significantly from the crystalline packing. In fact, when computational models are terminated at the methyl of the phenyl-alkoxy portion (Fig. S2, SI), the RMSD results drastically improve (Table 1). Although a statistical tool like RMSD can help provide a global picture of atomic coordinates (especially taking into account the diverse conformational movements of lateral aliphatic arms), the dihedral angle involving the chiral modules (2,2′-tethered binaphthyl for model 1, 1,1′-spirobiindane for model 2 and 3, and 9,9′-spirobifluorene for model 4, Fig. S3, SI) could be a more convenient geometrical variable to discuss. In such circumstances, outcomes from Table 1 enable several broad conclusions to be made about the impact of the distinct functionals employed. CAM-B3LYP and LC-ωHPBE showed the best performances (both in terms of RMSDs and dihedral angles) while the rest of the functionals exhibited slightly worse deltas (Table 1 and Fig. S4–S6, SI). This closer examination confirms that the incorporation of long-range correction terms (CAM-B3LYP and LC-ωHPBE) is important for recreating non-planar highly π-conjugated backbones whose electron clouds can interact both through bonds and through space.

2.1. Case 1: binaphthyl tethered helical ladder polymer (Pol1)

Having established our dominant functional (CAM-B3LYP) for the ground state description of ladderization monomers, we chose to start with the helical ladder polymer built from compound 1 (Fig. 2) as a computational reference to extend our DFT findings to progressively more extended oligomeric/

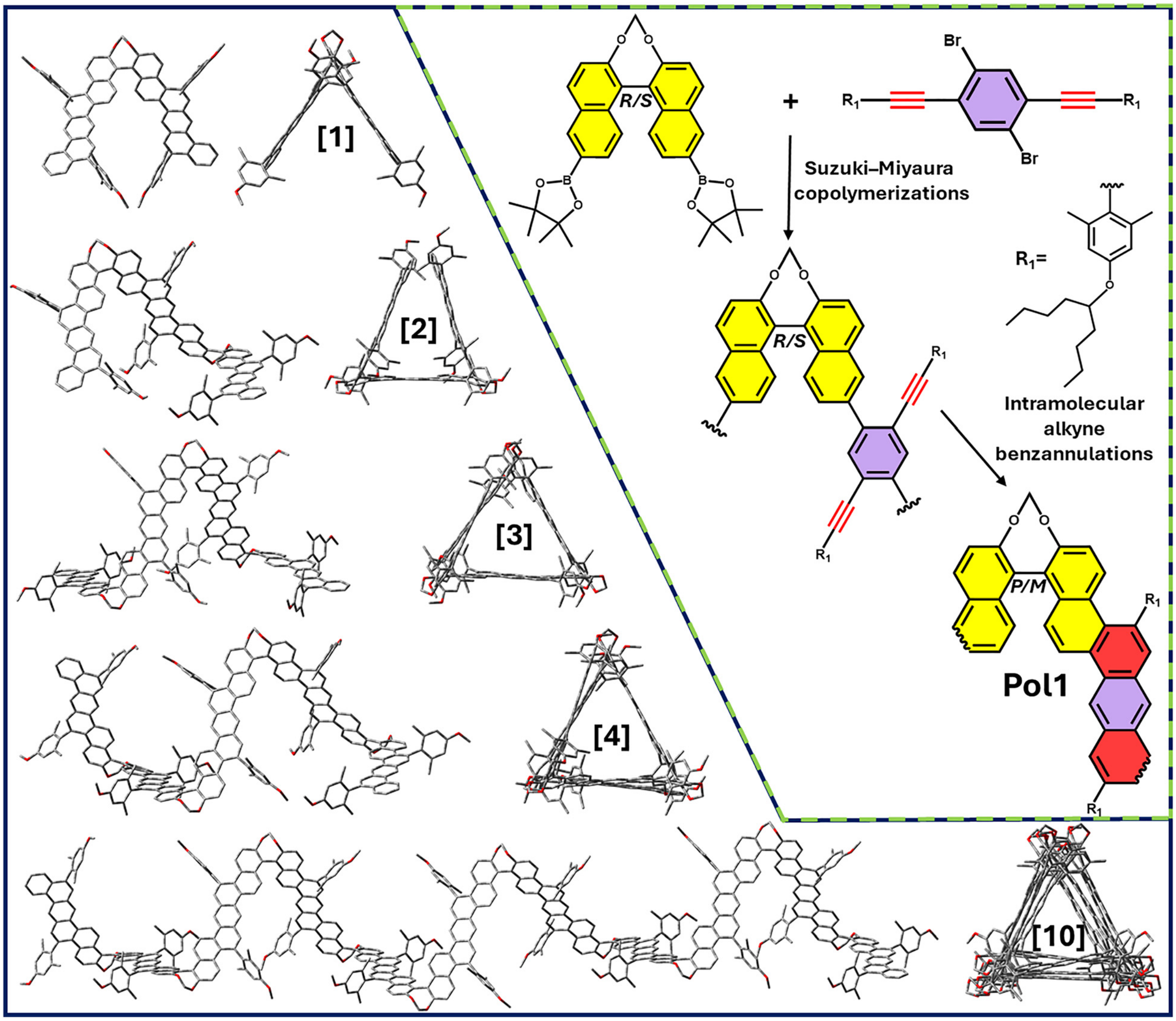

Fig. 3 (Left) Optimized models (Pol1[1], Pol1[2], Pol1[3], Pol1[4] and Pol1[10]) at the CAM-B3LYP/6-311G(d,p) level in the gas phase (for convenience only *S*/*M* forms are depicted). For clarity, hydrogens were omitted. (Right) Step-by-step synthetic pathway for Pol1. Colour labelling is consistent with Fig. 1 and 2.

polymeric chains. Ikai *et al.* ingeniously capitalized the incorporation of a single-handed axially chiral 1,1′-binaphthyl tethered (methylenedioxy) at the 2,2′-positions into a defect-free tubular macromolecular environment through a chemo- and regio-selective acid-promoted alkyne benzannulation (cyclization occurs at the 5,5′-positions of the 1,1′-binaphthyl biaryl frame) of the ethynyl functions of 2,6-dimethyl-substituted 4-alkoxyphenyl pendants. *De facto*, an initial Suzuki–Miyaura coupling copolymerization and successive chemo-controlled intramolecular annellations enantioselectively produced *M* (from (*S*) 1,1′-binaphthyl) and *P* (from (*R*) 1,1′-binaphthyl) helical ladder polymer (Fig. 3). In light of this, we designed five different models to thoroughly scrutinize how circularly polarized emission varies when the polymer length increases. Each structure was labelled according to the number of binaphthyl cores (square brackets), while the π-platforms were truncated with a closing fused benzene ring (the end-group effect should be imperceptible in a polymeric system). Finally, to speed up the calculations, the butoxy segments of the lateral alkoxyphenyl arms were reduced to methoxy groups (equivalently to the monomeric truncated forms, Fig. S2, SI). Global minima found for Pol1[2], Pol1[3], Pol1[4] and Pol1[10] confirmed that the dihedral angle value of monomer 1 (Pol1[1], Fig. 2) is regularly transferred to larger models (Table S1, SI), while the methylenedioxy spacer between the bis-aryl blades imposes a triangular secondary structure (Fig. 3) with a helical pitch of 2.66 nm retained all along the cyclic models (Table S1, SI). This shows that the scale-effect perfectly aligns with the monomer's geometrical modulation, but the chiral size-effect, possibly affecting the CPL spectra, remains unclear. For this reason, the light-activated chiral states of each theoretical prototype were interrogated photodynamically using excited-state molecular dynamics to take into account the thermal-dependent movements with the photoexcitation process. Persuaded by our DFT examination, the phase space conformational samplings of the first excited state (S1) for Pol1[1], Pol1[2], Pol1[3], Pol1[4] and Pol1[10] were acquired at the CAM-B3LYP/6-311G(d,p) level to obtain a clear depiction of the potential energy surfaces in S1 over a picosecond scale and to comprehend how local geometrical parameters (dihedral angles) and a more global feature (helical pitch) affecting the secondary structure vary during the electronic transition.

The analysis of S1 trajectories highlighted a moderate decrease in the dihedral angle ($\Delta\varphi \sim$ 4–5°) along all the oligostructures compared to the relative S0 values (Fig. S7, SI), which in turn reflects a small but perceptible reduction in the helical pitch ($\Delta\Omega \sim$ 1 Å, Fig. S8, SI). These data certify that the triangular geometrical integrity of the ground state is also entirely retained in the first singlet excited state without appreciable uncoiling. Before assessing the chiral consequences of the aforementioned structural responses, we also studied two new Pol1 variants (which emerged from the synthetic routes involving ethylenedioxy and propylenedioxy tethered binaphthyls, Fig. S9, SI). The progressive inclusion of CH_2 blocks in the alkylenedioxy spacer enlarged the twisting angle (φ) between the naphthyl platforms, introducing a more complex polygonal secondary structure (Fig. 4). DFT energy minima for [Et]Pol1[1] and [Pr]Pol1[1] monomers displayed equivalent φ values (~66°, Table S2, SI) because of a more flexible alkylenedioxy member. This chemical modification was also computationally surveyed in its elongated forms ([Et]Pol1[10] and [Pr]Pol1[10]), demonstrating peculiar discrepancies between the two cases (Table S2, SI). Indeed, the semi-flexible ethylenedioxy chain maintains the same ϕ angle in both the monomer and the polymeric species (practically, the "V" monomeric shape is invariably repeated in the elongated system). Conversely, the more adjustable propylenedioxy fragment did not preserve the monomeric ϕ angle in its polymeric module; in fact a 75° φ value conferred a more gyratory helical secondary structure (Fig. 4). Likewise, the helical pitches of [Et]Pol1[10] and [Pr]Pol1[10] underwent a contraction ($\Delta\Omega \sim$ 0.8 nm) compared to Pol1[10] (Table S2 and Fig. S8, S10, SI), owing to intramolecular hydrogen bonds (which compress the spring segments engaging the alkoxyphenyl peripheral pendants, Fig. S11, SI) facilitated by a superior disarticulation effect. These data corroborate the previous molecular mechanical (MM) calculations on the same polymer types,[25] which correctly assigned the dihedral angles and topological shapes but were quite insensitive to through-space electrostatic interactions, producing invariable helical pitch measurements (2.5–2.7 nm) for the three forms. The evolution of dihedral angles and helical pitches in the first singlet excited state of [Et]Pol1[10] and [Pr]Pol1[10] assumed a marginal shrinkage for both parameters (Table S2 and Fig. S8, S12, SI).

Once the S1 runs were rationalized, we utilized the related excited trajectories to implement a TD-DFT plan designed for extracting the size-dependent chiroptical contribution of all of the length-scalable models from the CPL spectra. A plethora of exchange–correlation functionals (B3LYP, APFD, B3PW91, CAM-B3LYP, ωB97XD, mPW1PW91, LC-ωHPBE, O3LYP, B97D3, HCTH, M11L, PBEPBE and TPSSTPSS) were then used to capture all the elements (emission energies, oscillatory and rotatory strengths, transition dipole moments, *etc.*) necessary to delineate the CPL spectral profiles. Considering that the optical status (peak position and band shape) should be transferable across increasingly longer species, for computational convenience Pol1[1] was accepted as a starting model as the basis for assessing the performance of the functionals. Remember that the one-handed helical ladder polymer (Pol1, Fig. 5B) disclosed an experimental CPL maximum in the 420–450 nm range. Fig. 5A reveals significant differences in the performances of the functionals. First and foremost, five functionals (B97D3, HCTH, M11L, PBEPBE and TPSSTPSS) registered a silent signal caused by very low rotational strengths (approximately null R length values, Table S3, SI), while the rest of the functionals presented active CPL lines with the correct chiral signs (positive for the *R* and negative for the *S* enantiomers). CAM-B3LYP, ωB97XD and LC-ωHPBE populated the high-frequency range (~340–380 nm) with sharp Gaussian band shapes, while the maximum for mPW1PW91 is located in an intermediate region, but the related spectrum still conserves a peaked pattern. B3LYP, APFD, and B3PW91 undoubtedly occupy the salient part of the visible spectrum with very accurate wavelength emissions (434 nm, 425 nm and 432nm, respectively) and credible pseudo-Gaussian band shapes. Although a direct comparison between experimental and theoretical CPL intensities is very hard (eqn (5) is expressed in molecular quantities, *i.e.*, it furnishes the CPL intensity for each emitting molecule, whereas experimentally, besides the instrumental settings, the CPL magnitude depends on the excited-state population, which is very difficult to estimate), a qualitative evaluation (in terms of order of magnitude) can be mentioned. Indeed, it is unrealistic that the computed B3LYP,

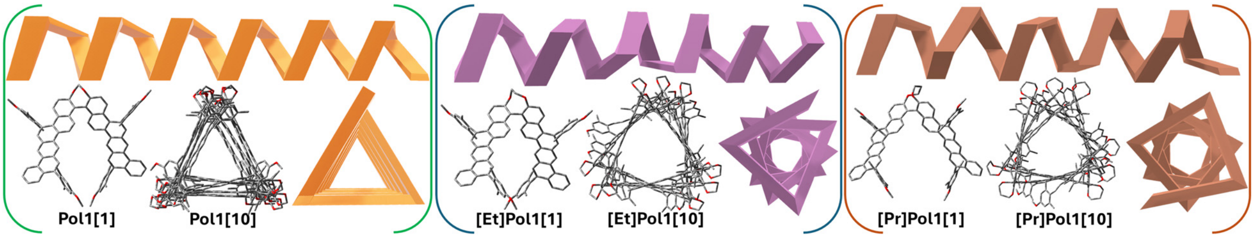

Fig. 4 Stylized classification of the different internal helical shapes for Pol1[10], [Et]Pol1[10] and [Pr]Pol1[10]. For clarity, hydrogens were omitted.

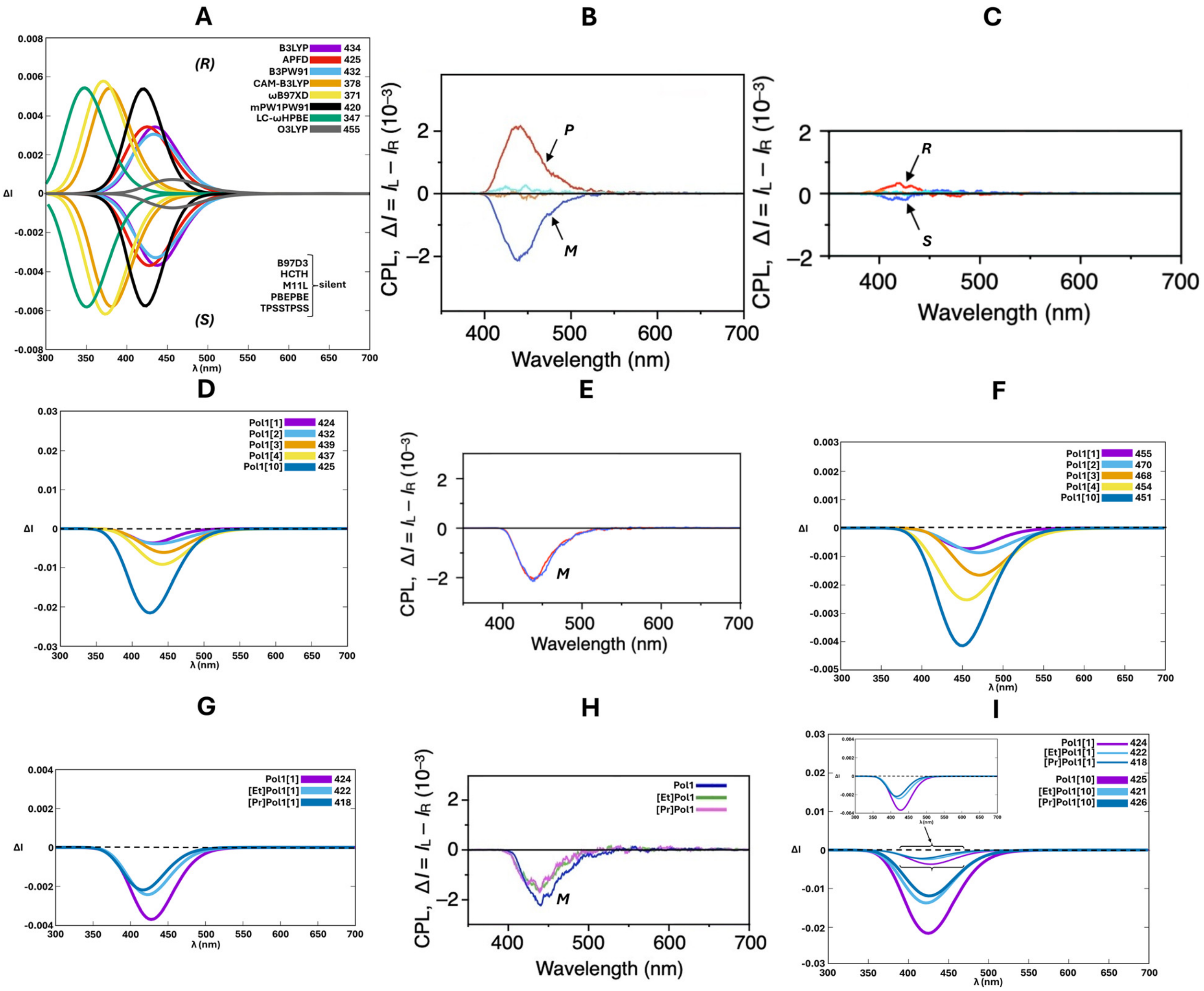

Fig. 5 (A) Overview of the TD-DFT-predicted CPL spectra at the functional/6-311G(d,p) level along the excited trajectories for (*R*)/(*S*)-Pol1[1] in chloroform. (B) Experimental CPL spectra for (*P*)/(*M*)-Pol1 in chloroform (quasi-silent signals refer to unzipped polymers, see Fig. 3, synthetic step 1). Reproduced with permission from ref. 25 © 2024. Wiley-VCH Verlag GmbH & Co. KGaA. (C) Experimental CPL spectra for (*R*)/(*S*)-Pol1[1] in chloroform. Adapted with permission from ref. 25 © 2024. Wiley-VCH Verlag GmbH & Co. KGaA. (D) Assemblage of the TD-DFT predicted CPL spectra at the APFD/6-311G(d,p) level along the excited trajectories for the (*S*/*M*) forms of Pol1[1], Pol1[2], Pol1[3], Pol1[4] and Pol1[10] in chloroform. (E) Experimental CPL spectra for (*M*)-Pol1 in chloroform (red curve and the blue one refer to 0.01 M and 0.1 M, respectively). Adapted with permission from ref. 25 © 2024. Wiley-VCH Verlag GmbH & Co. KGaA. (F) TD-DFT predicted CPL spectra at the O3LYP/6-311G(d,p) level along the excited trajectories for the (*S*/*M*) forms of Pol1[1], Pol1[2], Pol1[3], Pol1[4] and Pol1[10] in chloroform. (G) TD-DFT predicted CPL spectra at the APFD/6-311G(d,p) level along the excited trajectories for the (*S*) forms of Pol1[1], [Et]Pol1[1] and [Pr]Pol1[1] in chloroform. (H) Experimental CPL spectra for (*M*)Pol1[1], (*M*)[Et]Pol1 and (*M*)[Pr]Pol1 in chloroform. Adapted with permission from ref. 25 © 2024. Wiley-VCH Verlag GmbH & Co. KGaA. (I) TD-DFT predicted CPL spectra at the APFD/6-311G(d,p) level along the excited trajectories for the (*S*/*M*) forms of Pol1[1], [Et]Pol1[1],[Pr]Pol1[1], Pol1[10], [Et]Pol1[10] and [Pr]Pol1[10] in chloroform; insert is related to (G).

APFD and B3PW91 ΔI for monomeric Pol1[1] ($\sim$0.0035) are roughly correspondent to experimental values for the Pol1 polymeric system (Fig. 5B). In this scenario, the slightly red-shifted O3LYP spectrum (455 nm) fits very well, presenting more reasonable rotational strengths (Table S4, SI), with satisfactory band intensity, being sufficiently adherent to the experimental Pol1[1] CPL spectrum (Fig. 5C). From the above arguments, it is clear that B3LYP, APFD and B3PW91 accurately reproduce the peak positions while O3LYP mimics the chiroptically quiet behaviour of Pol1[1]. APFD (arbitrarily elected as a representative member of the ternary group functionals) and O3LYP were then chosen to determine how the number of repeating units contributes to the final CPL intensity in a size-scalable model (for convenience, the *S*/*M* form was checked). Moving along the models, APFD CPL peaks are condensed in a narrow (424–439 nm, Fig. 5D) range, which exactly reproduces the experimental data (Fig. 5E), while O3LYP suffers a modest blue shift (451–470 nm), corroborating that the pure monomeric optical features are maintained across variable-size helical ladder systems. Both APFD and O3LYP calculations (Fig. 5D and F) offered an incremental augmentation in the CPL intensity by transitioning from Pol1[1] to Pol1[10], derived from the sequential increase of rotational strength (*R* length values, Table S4, SI), which can be justified by the bidirectional growth of the chiral entities (binaphthyl tethered cores) along the helical ladder polymer. Although the two intensity trends are qualitatively analogous (Pol1[1] < Pol1[2] < Pol1[3] < Pol1[4] < Pol1[10]), APFD reported exaggerated chiral signals that exceeded the experimental data by an order of magnitude, while on the contrary, O3LYP localizes their spectra in an acceptable intensity region (Fig. 5D–F). Data fitting of these hierarchical chiral signals *versus* the asymmetric units (binaphthyl tethered scaffolds) was elaborated and, even if a preliminary linear regression denoted a good correlation (Fig. S13, SI), a subsequent hyperbolic decay function finely interpolated the computed rotational strengths. Although this is admittedly a semi-quantitative approach (caused by issues in theoretical/experimental intensity matching), such outcomes indicate that a decreasing (or increasing for the opposite enantiomer) exponential trend, which asymptotically reaches a plateau, is a more realistic description than linear proportionality, which presumes an indefinite increase in CPL intensity as the number of chiral nodes increases (although in the smallest oligomers, direct proportionality can be extrapolated). This type of chiroptical convergence faithfully follows the tendency of experimental anisotropy values (g_{abs}) observed for helical triptycene-based π-conjugated ladder polymers.[34] At this point, a logical question spontaneously arises: what happens if the alkylenedioxy linker, and accordingly the helical channel topology, is modified? Experimental CPL spectra (Fig. 5H) showed a gradual CPL intensity down-shift moving from Pol1 to [Pr]Pol1 one-handed helical ladder polymers. Confident of the transferability of our two DFT levels, APFD and O3LYP were implemented for the Pol1[1], [Et]Pol[1] and [Pr]Pol[1] monomeric precursors. Fig. 5G (and Fig. S14, SI) shows that, although the two functionals appropriately identify the correct experimental intensity hierarchy (Pol1 > [Et]Pol1 > [Pr]Pol[1]) in terms of their order of magnitude, APFD in particular precisely catches both the wavelength interval (418–424 nm) and the intensity ratio among the three monomeric derivatives, while O3LYP showed a bigger intensity spacing and a tolerable blue shift (Fig. S14, SI). Excepting wavelength micro-fluctuations, APFD simulations of Pol1[10] [Et]Pol1[10] and [Pr]Pol1[10] polymeric structures showed that the related intensities are proportionally reinforced, preserving the correct CPL signal order (Fig. 5I and Table S5, SI). Given that the number of chiral units is equal within the two subgroups (one for Pol1[1]/[Et]Pol1[1]/[Pr]Pol[1] and 10 for Pol1[10]/[Et]Pol1[10]/[Pr]Pol[10]), the disparity in the ΔI should be attributed to the different chiroptical transition characteristics derived from the installed methylene, ethylene or propylene di-oxy segments. From meticulous scrutiny of the monomeric molecules, it seems that a longer alkylenedioxy chain tends to restrict the angle between the electric and magnetic transition dipole moments toward a right angle disposition (during the S1–S0 radiative process, Table S6 and Fig. S15, SI), which leads to smaller cosine values, causing a decrease in rotatory strength, according to the Rosenfield equation (eqn (S1), SI). This effect, mutually assisted by the amplification of transition dipole moments, was also boosted for Pol1[10], [Et]Pol1[10] and [Pr]Pol1[10] (Fig. S16 and Tables S6, S7, SI).

2.2. Case 2: Pol2, Pol3, Pol4 and Pol5

Ikai's group brilliantly took advantage of quantitative and chemoselective acid-promoted intramolecular annulations to integrate the spiro nodes into conjugated ladder polymers, obtaining definite and predictable primary and secondary structures.[26–28] Elegantly, the reaction site designation of the acid-induced electrophilic intramolecular multicyclization triggers unique orthogonally-bridged spiro-conjugated molecular reels with exclusive helical cavity topologies. Chronologically speaking, the first single-handed helical spiro-conjugated ladder polymer involved a starting spiro-type asymmetric linkage between an axially chiral (4,4′)-1,1′-spirobiindane-based diboronic ester and a *p*-dibromo(diethynyl)benzene derivative, followed by acid-mediated intramolecular benzannulations. In the final structure (Pol2, Fig. 6), the orthogonally connected dibenzo[a,h]anthracene units provided a helical rigid rod with an univocally recognized chirality (*M*/*P* sense depending on *S*/*R* spirobiindane precursor). In view of the tremendous amount of ladder backbone atoms, we proposed a Pol2[7] model to computationally elucidate the structure–chiroptical relationship. The DFT optimization on Pol2[7] proclaimed a monodirectional zig-zag geometry, which altered the polymer dihedral angle values (Table S8, SI), and a helical pitch of 2.51 nm. Excited-state trajectory accumulations certified the extremely tightly twisted three-dimensional architecture through an unvarying dihedral angle between S0 and S1 (Fig. S17, SI), thus imposing strictly limited conformational freedom to the whole polymeric system.

An appealing variant of Pol2 was actuated with a complementary synthetic route in which a (6,6′)-1,1′-spirobiindane-based dibromo derivative reacted with a *p*-diboronic-(diethynyl)benzene ester to obtain a different linkage position in the coupling intermediate, which, after the benzannulation step, entailed consecutively fused rectangular platforms with a cylindrical cavity (Pol3, Fig. 6). Pol3[8] energy minimization revealed a slightly larger dihedral angle compared to the Pol3[1] counterpart (Table S8, SI), probably to accommodate an important cavity shape in its polymeric form. It is worth pointing out that the Pol3 series (polymeric and monomeric species) possesses a more torsioned spirobiindane module; although the spiro-linked hydroxy (Pol3) and ethoxy (Pol2) groups scarcely influence it, the main contribution can be credited to the "endo" (Pol3) anthracene arrangement, which requires a more orthogonal disposition to minimize the steric hindrance than the "exo" (Pol2) one (Fig. 6 and Table S8, SI). Pol3 S1 dynamics exhibited dihedral angle enlargement in both Pol3[1] and Pol3[7], generating a more expanded rectangular cavity (Fig. S18, SI).

Similarly, Pol4 exhibited a helical superstructure thanks to a spiro bicyclic system. In fact, a Suzuki C–C coupling reaction between a (2,2′)9,9′-spirobifluorene diboronate compound and a dibromo(diethynyl)phenylene comonomer, followed by acid-

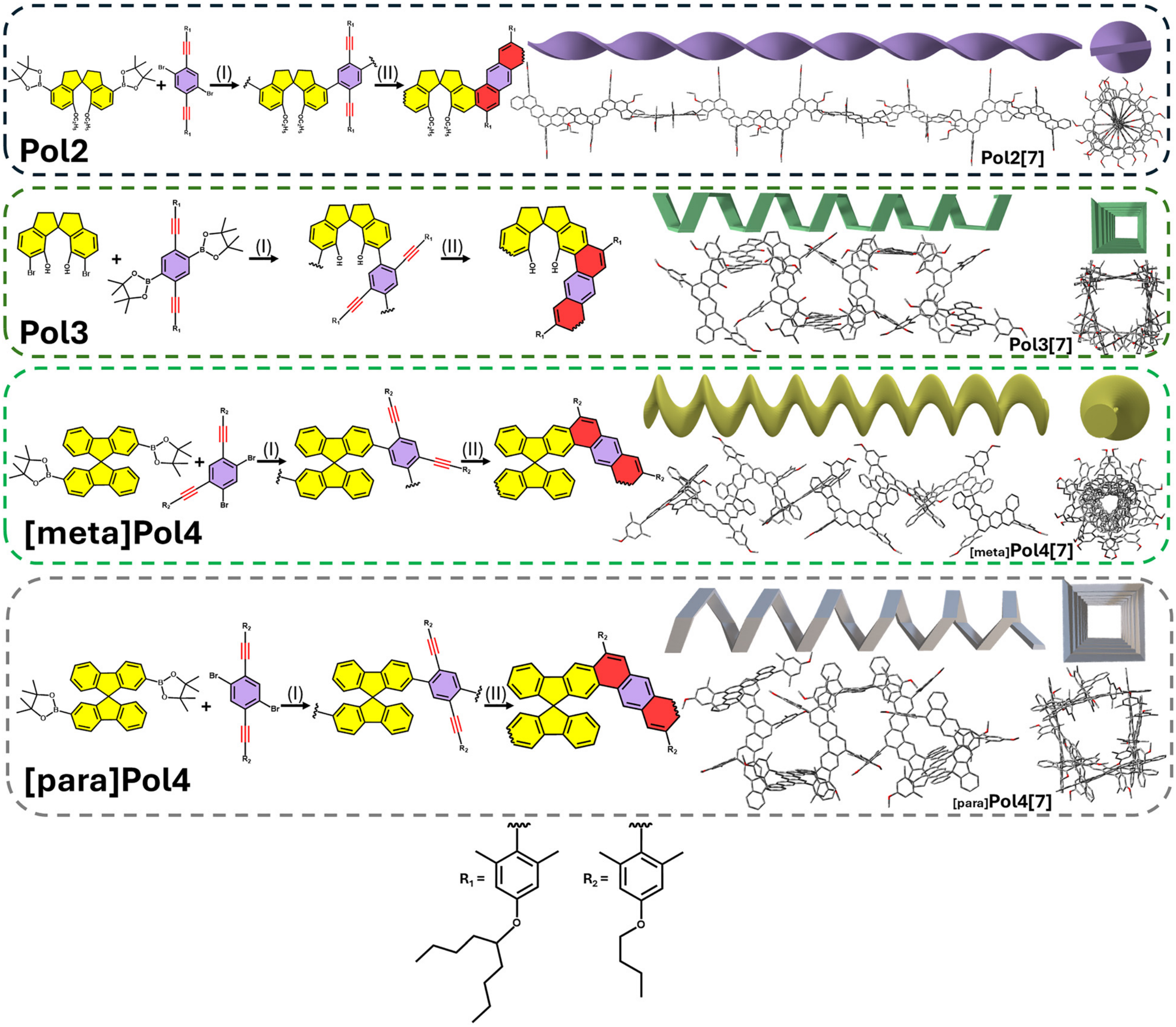

Fig. 6 (Left) Synthetic conceptualization of Pol2, Pol3, [*meta*]Pol4 and [*para*]Pol4. (Right) Lateral and frontal view of optimized (*P*)Pol2[7], (*P*)Pol3[7], (*P*)[*meta*]Pol4[7] and (*M*)[*para*]Pol4[7]. It must be noted that the central void in the [*meta*]Pol4[7] compound is not a cavity but rather a consequence of the alternating arrangement of the repeating units. Steps (I) and (II) refer to Suzuki–Miyaura copolymerization and alkyne intramolecular benzannulation, respectively. For clarity, hydrogens were omitted.

assisted annulations, encapsulated cyclic repeating units, endowing global spiral asymmetry (Fig. 6). In this case, the cavity topology was dependent on the dibromo position in the dialkynylphenylene unit (while in Pol2 and Pol3 the chemical modifications regarded the spiro core); *para*-branching led to a helical tubular channel, while meta-branching led to cavity-free helical grooves. Computed [*para*]Pol4[7] minima exemplified unchanged dihedral angle values in comparison to its monomeric axle ([*para*]Pol4[1], Table S8, SI), while [meta]Pol4[7] delineated a distinguishable ϕ expansion. This condition of almost perfect ϕ orthogonality in [meta]Pol4[7] could be explained by the necessity of having a rigid zig-zag (and cavity-free) structure to relax the hindered environment between the spirobifluorene pales and the 2,6-dimethyl substituted 4-alkoxyphenyl pendants (Fig. S19, SI). Such an effect is also reflected in the excited state, where [*para*]Pol4[1] and [*para*]Pol4[7] conserved the S0 dihedral angle while [*meta*]-Pol4[1] and [*meta*]Pol4[7] augmented the twisted angles in the spirobifluorene nuclei (Fig. S20, SI).

Having examined the structures of all of the cavity-endowed ladder polymeric cases (Pol1, Pol3 and [*meta*]Pol4), it is clear that, although the anthracene segment is the same, the cavity volume strictly depends on the axial chiral module (binaphthyl tethered, spirobiindane and spirobifluorene) and on the benzannulation reaction sites, which in turn regulate the internal topology (Fig. S22, SI).

From a chiroptical perspective, although Pol2, Pol3 and Pol4 exhibit different helical configurations, their luminogenic activity centers the experimental chiral emissions in a narrow range (CPL maxima range between $\sim$420–450 nm, Fig. 7B, D, F, G and H). Systematically moving across the computational models (Pol2[7], Pol3[7], [*meta*]Pol4[7] and [*para*]Pol4[7]), it is worth mentioning that the aforementioned transferable performance of APFD and O3LYP was maintained. In fact, in every case, APFD moderately blue-shifted the CPL peak positions while O3LYP aptly simulates the CPL maxima wavelength (Fig. 7A, C and E), displaying accurate spectral profiles. As for the Pol1 series (Fig. 5), APFD tends to overestimate the chiral intensities, while the calculated O3LYP rotational strengths provided more realistic CPL signals. On this matter, initially focusing on Pol2[7] and Pol3[7] (and their related experimental counterparts, Pol2 and Pol3 Fig. 7B and D), it is possible to see that the helical topology dictates the CPL chiral amplitude, assigning more intense signals (higher *R* length values, Table S9, SI) for helical tubular Pol3[7] than helical ribbon-like Pol2[7] (this effect was also verified by the hydroxy-analogous Pol2 helical ladder polymer, Pol5 Fig. S23, SI). Up to this point, (*R*) and (*S*) monomers automatically produced (*P*) and (*M*) helical ladder polymers, respectively. Curiously, (*R*)[*para*]Pol4[1] monomer triggers *M* helicity (hence (*S*)[para]Pol4[1] activates *P* helicity) while (*R*)[*meta*]Pol4[1] induces *P* helicity (hence (*S*)[*meta*]Pol4[1] activates *M* helicity), resulting in the first example of an enantiomerically resolved precursor that provokes inverted helicity in single-handed helical ladder polymers. In this instance, the absence of a helical cavity (meta polymers, Fig. 7F and H) controls the CPL fingerprint, significantly exceeding the tubular-cavity alternative (para polymers, Fig. 7G) in terms of intensity. Our best-performing functionals responsively reacted to this chirality inversion, providing a net intensity decrement when the para system was TD-computed (Fig. 7E and Table S10, SI) with silent (O3LYP) or very weak signals (APFD). This can be explained by observing electric and magnetic transition dipole moments and their angles, whose values are maximized in meta polymers, while para configuration significantly lowers the transition vectors (Table S11, SI). Surprisingly, Pol4 CPL intensities (high values for cavity-free polymers) were reversed compared to those of Pol3 (high values for tubular-cavity polymers), both experimentally and theoretically, demonstrating that the choice of chiral inducer and ladder orientation intimately affect the electric and magnetic transition features, which affect the rotational strength.

2.3. Electronic transition analyses

A careful readthrough of the data for Pol1, Pol2, Pol3, Pol4 and Pol5 suggests that all the single-handed helical ladder polymers can be structurally rationalized as trimodular systems: (1) a chiral node that represents a source of asymmetry (yellow module, Fig. 3, 6 and Fig. S23, SI); (2) anthracene axles derived from the ladderization process (red and blue blades, Fig. 3, 6 and Fig. S23, SI); (3) 2,6-dimethyl-substituted 4-alkoxyphenyl arms are necessary to chemoselectively guide the synthetic step toward a defect-free product (R_1 and R_2 pendants, Fig. 3, 6 and Fig. S23, SI). Hence, a vast range of chemical components (and their possible combinations) can govern the electronic transition on the photoexcitation pathway. Convinced that the monomeric electronic properties are periodically disseminated along the polymeric forms, the frontier orbitals (HOMO and LUMO) of Pol1[1], Pol2[1], Pol3[1] and [meta]Pol4[1] were plotted. Progressing from Pol1[1] to [meta]Pol4[1], both orbital functions envelope the fused-polyarene platforms, affirming a typical π–π* transition. Fig. S24 clearly shows that the electron clouds of 2,6-dimethyl-substituted 4-alkoxyphenyl lateral chains do not participate by reason of orthogonally interrupted π-communications; such an effect is also manifested in the spiro-bridged cyclopentane rings (Pol2[1], Pol3[1] and [meta]-Pol4[1]). In this sense, the chiral center of Pol1[1] is an exception since the binaphthyl site is entirely fused to the anthracene and only the alkylenedioxy arc is excluded from the HOMO and LUMO orbitals. Beyond this qualitative analysis, it remains unknown which atomistic section predominantly determines the electronic transition and duly affects the spectral characteristics. In this vein, the transition density matrix (TDM) can support us in unambiguously distinguishing the various contributions (to the photoexcitation) from the different atomic/molecular zones. TDM between S0 and S1 for our N-electron Pol1[1], Pol2[1], Pol3[1] and [meta]Pol4[1] monomers in the real space representation can be expressed as:

$$T(r;r') = \int \tau^0(X_1X_1 \ldots X_n)\psi_\mathrm{e}(X_1X_2 \ldots X_n)\mathrm{d}\varrho_1(\mathrm{d}X_1\mathrm{d}X_2 \ldots \mathrm{d}X_n) \tag{1}$$

where τ^0 is the S0 real-type wavefunction Slater determinant, ψ_e is the excited-state wavefunction, and X and ϱ are the spin-space and spin coordinates, respectively. If the Slater–Condon rule is applied to the expanded ψ_e, TDM can be reformulated as follows:

$$T(r;r') = \sum_\mathrm{o}\sum_\mathrm{v} C_\mathrm{o}^\mathrm{v}\varphi_\mathrm{o}(r)\varphi_\mathrm{v}(r') \tag{2}$$

For only diagonal terms, eqn (2) becomes:

$$T(r) = \sum_\mathrm{o}\sum_\mathrm{v} C_\mathrm{o}^\mathrm{v}\varphi_\mathrm{o}(r)\varphi_\mathrm{v}(r) \tag{3}$$

Now $T(r)$ can be treated as a real space function where o and v indexes cover all occupied and virtual molecular orbitals, respectively. φ_o and φ_v are the configuration state wavefunctions for occupied and virtual molecular orbitals and C_o^v is the configuration coefficient. Reasonably assuming that the electronic excitation invests the HOMO–LUMO transition, $T(r)$ is simply:

$$T(r) = C_\mathrm{homo}^\mathrm{lumo}\varphi_\mathrm{HOMO}(r)\varphi_\mathrm{LUMO}(r) \tag{4}$$

This equation tells us that, if an atomic/molecular region has a high transition density value, the photogenerated hole–electron couple will be localized in that chemical area. On the other hand, a small contribution to $T(r)$ presupposes irrelevant hole–electron overlap in that zone. For our scope, both atomic (ATDM) and fragment (FTDM) transition density matrices were processed ignoring the hydrogens since they infrequently exert influence on the electronic transitions. ATDM (Fig. 8), through nucleus-by-nucleus data, informs us that two distinct specular patterns are associated with the larger hole–electron

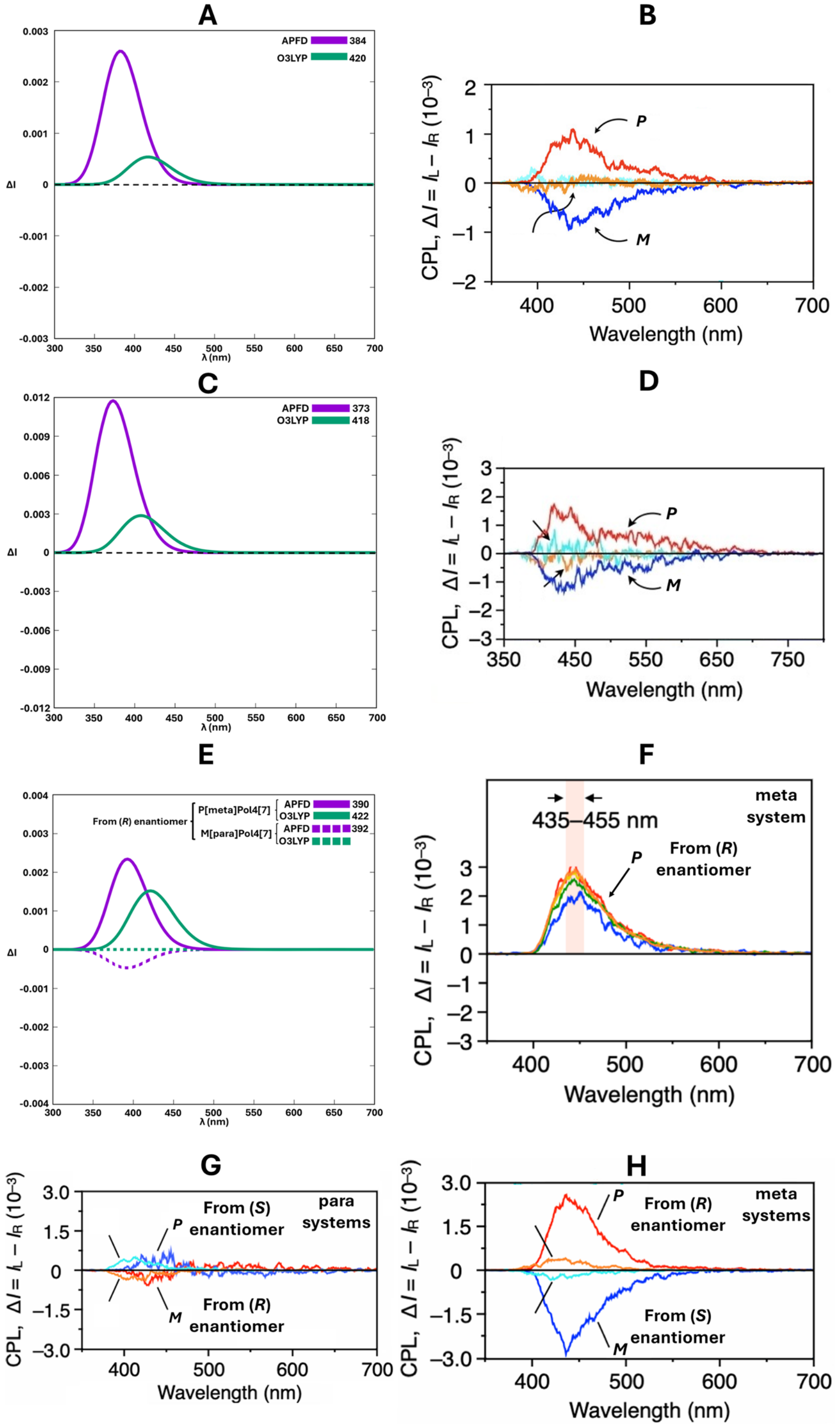

Fig. 7 (A) APFD and O3LYP TD-DFT predicted CPL spectra along the excited trajectories for (*P*)-Pol2[7] in chloroform. (B) Experimental CPL spectra for (*P*)/(*M*)-Pol2 in chloroform (quasi-silent non-specified signals refer to unzipped polymers, see Fig. 6, synthetic step 1). Reproduced with permission from ref. 26 © 2021. Wiley-VCH Verlag GmbH & Co. KGaA. (C) APFD and O3LYP TD-DFT predicted CPL spectra along the excited trajectories for (*P*)-Pol3[7] in chloroform. (D) Experimental CPL spectra for (*P*)/(*M*)-Pol3 in chloroform (quasi-silent non-specified signals refer to unzipped polymers, see Fig. 6, synthetic step 1). Adapted with permission from ref. 27 © 2023. Wiley-VCH Verlag GmbH & Co. KGaA. (E) APFD and O3LYP TD-DFT predicted CPL spectra along the excited trajectories for (*P*)-[meta]Pol4[7] and (*M*)-[para]Pol4[7] in chloroform. (F) Experimental CPL spectra for (*P*)[meta]Pol4 in chloroform (colours refer to different eluted fractions during the purification). Adapted with permission from ref. 28 © 2025. American Chemical Society. (G) Experimental CPL spectra of (*P*)/(*M*)[*para*]Pol4 in chloroform (quasi-silent non-specified signals refer to unzipped polymers, see Fig. 6, synthetic step 1). Adapted with permission from ref. 28 © 2025. American Chemical Society. (H) Experimental CPL spectra for (*P*)/(*M*)[meta]Pol4 in chloroform (quasi-silent non-specified signals refer to unzipped polymers, see Fig. 6, synthetic step 1). Adapted with permission from ref. 28 © 2025. American Chemical Society.

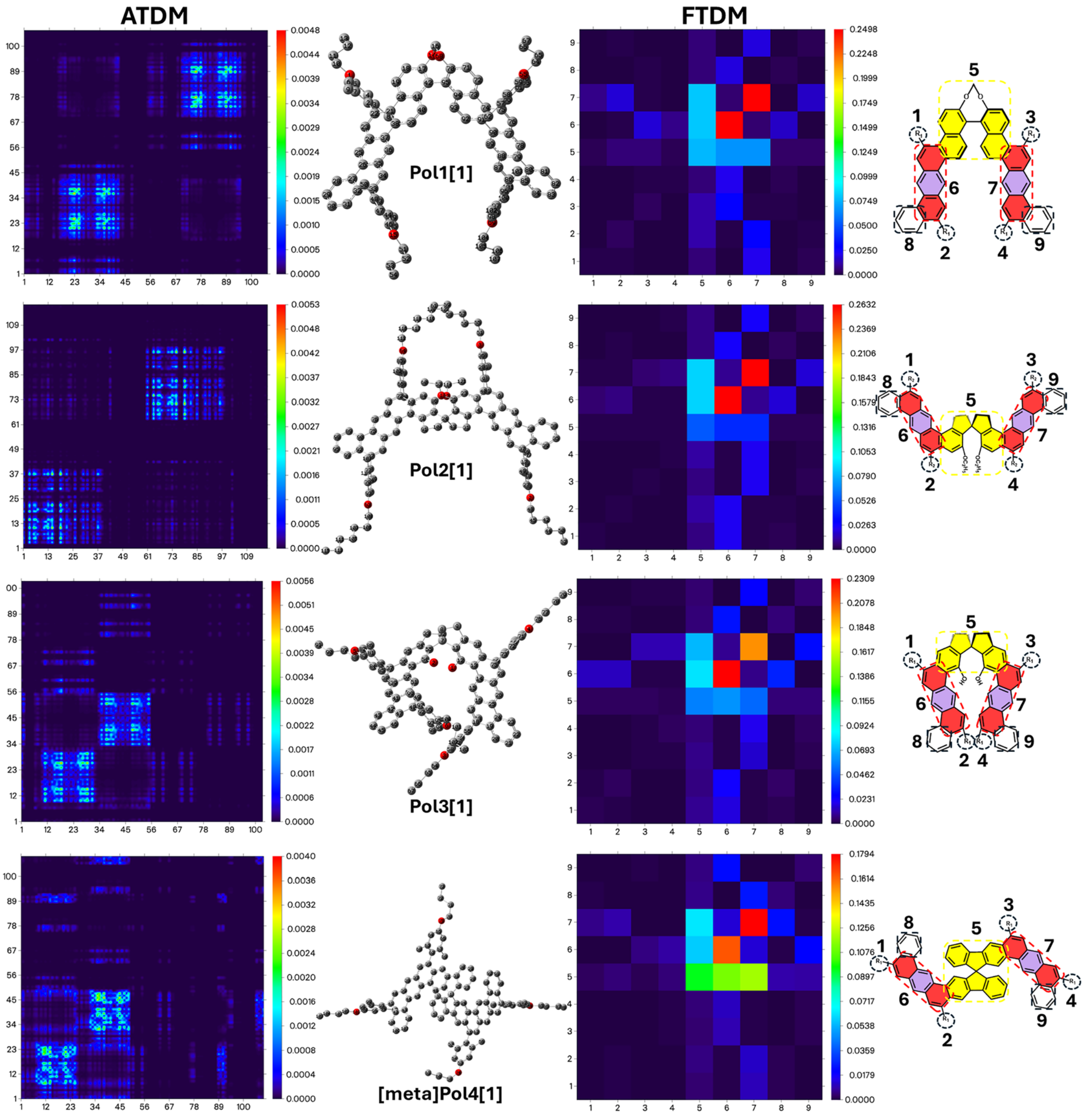

Fig. 8 Atomic (left) and fragment (right) transition density matrix maps for Pol1[1] Pol2[1] Pol3[1] and [meta]Pol4[1]. Atomic indexes are reported in the ball and stick models, while fragment labels are coded in the molecule representations. It must be noted that X axes are intended as "holes" while Y axes are "electrons". For simplicity, [para]Pol4[1] and Pol5[1] were not reported because their 2D maps are identical to those of [meta]Pol4[1] and Pol2[1], respectively.

coherence for the systems inspected (Pol1[1], Pol2[1], Pol3[1] and [meta]Pol4[1]). Notwithstanding the atomic indexing, the large number of atoms caused dense yellow spots, which underlined how the hole–electron mobility is confined within the two anthracene axles (intense coloured region along the main diagonal, see atomic labels in Fig. 8). For each monomer, the ATDM map is complicated by intense off-diagonal matrix elements opposite to the anthracene-related spots, demonstring that the photoexcitation is not integrally restricted to the anthracene scaffolds. To scrupulously examine this aspect and obtain less crowded maps, fragment assignment became essential, and FTDM revealed a more comprehensible situation. Fig. 8 confirmed that the 2,6-dimethyl-substituted 4-alkoxyphenyl arms (fragments 1, 2, 3 and 4) have quasi-zero hole–electron distribution (blue spots on the diagonal), as do the closed rings (fragments 8 and 9), while the maximal FTDM values appeared for fragments 6 and 7 (orange/red squares, anthracene segments). Fragment 5 (chiral unit) exhibited an intermediate mode (cyan/yellow "L" diagram around the red squares), partially cooperating (with the anthracene part) in the hole–electron delocalization through its fused benzene ring and justifying the presence of relevant off-diagonal elements in the ATDM map. Ultimately, the optical features of these chiral excitations are attributed to the anthracene portions, which, as a single molecule has a structured emission spectrum between 400 and 450 nm,[58,59] corroborating the violet luminescence (400–450 nm band) rooted in the CPL single-handed helical ladder polymers.

3. Computational details

Deposited crystallographic coordinates of monomers 1,2,3 and 4 were taken from Cambridge Structural Database ($CCDC_1$: 2235867, $CCDC_2$: 2053268, $CCDC_3$: 2150478 and $CCDC_4$: 2394271) and analyzed in the gas phase using DFT *via* the following exchange–correlation functionals: B3LYP, CAM-B3LYP, TPSSTPSS, BLYP, B97D3, ωB97xD, mPW1PW91, MN12L, PW6B95D3 and LC-ωHPBE in combination with the 6-311G(d,p) Pople basis set, adopting a superfine grid and a tight criterion for energy and geometry optimization convergence (the same procedure was used for the truncated forms). Consequently, (*R*/*S*)Pol1[1], (*M*)Pol1[2], (*M*)Pol1[3], (*M*)Pol1[4], (*M*)Pol1[10], (*M*)[Et]Pol1[1], (*M*)[Et]Pol1[10], (*M*)[Pr]Pol1[1], (*M*)[Pr]Pol1[10], (*R*)Pol2[1], (*P*)Pol2[7], (*R*)Pol3[1], (P)Pol3[7], (*R*)[meta]Pol4[1], (*P*)[meta]Pol4[7], (*R*)[para]Pol4[1], (*M*)[para]-Pol4[7], and (*P*)Pol5[7] were energy-minimized at the CAM-B3LYP/6-311G(d,p) level in the gas phase. Each model was subjected to excited Born–Oppenheimer molecular dynamics (BOMD) in the first electronic state (S1) at the CAM-B3LYP/6-311G(d,p) level at 298 K with a total accumulation time of 1 ps and a step size of 2 fs. (*R*/*S*)Pol1[1] computational models were TD-DFT scanned through the B3LYP, APFD, B3PW91, CAM-B3LYP, ωB97XD, mPW1PW91, LC-ωHPBE, O3LYP, B97D3, HCTH, M11L, PBEPBE and TPSSTPSS functionals (6-311G(d,p) basis set) (while the rest of the theoretical prototypes were TD-modelled by APFD and O3LYP), which served to recover the rotatory strengths (*R* length), excitation energies (λ), oscillator strengths (s), electric/magnetic transition dipole moments (μ_E/μ_M) and their angles (θ) necessary to construct the spectral profile. CPL spectra were then computed as weighted sums of the spectra calculated at the TD-DFT level on temporally equispaced (40 fs) molecular conformation snapshots (26) extrapolated from BOMD trajectories. When specified, the solvent conditions (state-specific vertical excitation model, VEM) were defined by using the integral equation formalism for the polarizable continuum model (IEF-PCM); the default parameters of Gaussian16 were utilized for the construction of the cavity, built as the envelope of interlocked spheres centered on each atom of the solute (chloroform: ε = 4.71). The CPL intensities (ΔI) were calculated as follows:[60]

$$\Delta I = \frac{16 {E_{\mathrm{emi}}}^3 \times R_{0\mathrm{m}} \times \rho(E_{\mathrm{emi}})}{3\hbar^4 \times c^3} \tag{5}$$

where $\hbar$ is the reduced Planck's constant, c is the speed of light, $\rho(E_{\mathrm{emi}})$ is the Gaussian band shape centered in the E_{emi} energy and $R_{0\mathrm{m}}$ is the rotational strength associated with the transition 0 ← 1 (expressed as *R* length). Eqn (1) is formulated in cgs units and the band shape was assumed as Gaussian with a bandwidth of 1500 cm^{-1}. All the computational runs were carried out by the Gaussian16 package.[61] Electric/magnetic transition dipole vectors were visualized with VMD software[62] and transition density matrices (TDM) were processed and plotted using Multiwfn code.[63] Cavity volumes (V_{occ}) were computed by means of two-probes mode with a small probe radius of 1.2 Å, a large probe radius of 5.0 Å, and a grid resolution of 0.2 Å, implemented in the Molovol code.[64]

4. Conclusions

In the current decade, an ingenious two-step synthetic procedure implying Suzuki copolymerization and alkyne intramolecular benzannulation brought to light a new class of CPL-active and defect-free one-handed helical ladder polymers. In this work, we investigated the chiral size dependence of the circularly polarized luminescence spectra in progressively more extended ladder-type helical polymers by means of *ab initio* methodology. An initial DFT benchmark clarified how the CAM-B3LYP exchange–correlation functional capably diversified the dihedral angle values imprinted in the chiral modules (2,2′-tethered binaphthyl, 1,1′-spirobiindane and 9,9′-spirobifluorene) of the crystallographically verified monomers ((*S*)-Pol1[1], (*R*)-Pol2[1], (*R*)-Pol3[1] and (*R*)-Pol4[1]). The use of the Pol1 series (Pol1[1], Pol1[2], Pol1[3], Pol1[4] and Pol1[10]) as a computational probe favoured the exploration of how local (dihedral angle) and global (helical pitch) variables were transmitted from the monomeric cores to gradually more expanded polymeric structures during photoexcitation. The APFD and O3LYP exchange–correlation functionals shared the stage when the CPL spectra were simulated, culminating in very precise peak positions for the former and accurate chiral intensities for the latter. Their sensitivity was also validated by comparison with ethylene/propylenedioxy tethered homologues, whose cavity shapes generate hierarchical CPL signals. The chirality-scale dependence of the CPL rotatory strengths in the Pol1 set was interpreted *via R* length values and transition dipole moments (electric and magnetic), which reciprocally expected a divergence from a linear proportionality between chiral chain length and CPL magnitude, putting forward a more plausible hyperbolic trend. Through their tubular, cylindrical and cavity-free internal environments, spiro-conjugated Pol4, Pol3 and Pol2 helical structures demonstrated that O3LYP responds perfectly when the CPL spectral profile is controlled by different helical morphologies. Lastly, a detailed electronic transition analysis (ATDM and FTDM) refined the puzzle of chiral emissive one-handed helical ladder polymers, emphasizing how the violet CPL was attributable to the anthracene-localized excitation. Although CPL-active ladder-type helical polymers are still in their infancy, the presented computational guide can support chemists in decrypting helical-handed luminescent functions through the anticipated pre-screening of chiral units and polyarene ladderization products, allowing direct control of the final CPL brightness and colour.

Author contributions

Giovanni Bella: conceptualization, methodology, software, data curation, validation, investigation, project administration, writing – original draft. Giuseppe Bruno: resources, supervision, writing – review & editing. Marco Milone: resources, supervision, writing – review & editing. Antonio Santoro: supervision, writing – review & editing visualization, resources.

Conflicts of interest

There are no conflicts to declare.

Data availability

Experimental CPL spectra were reproduced with permission from: (1) **https://doi.org/10.1002/anie.202318712** (Fig. 5A and C in the main article and Fig. S14 and S18 in the supplementary information); (2) **https://doi.org/10.1002/anie.202102885** (Fig. 4C in the main article); (3) **https://doi.org/10.1002/anie.202218297** (Fig. 3F in the main article); (4) **https://doi.org/10.1021/acs.macromol.5c00677** (Fig. 5C in the main article and Fig. S19D in the supplementary information). The datasets supporting this article and the relative code/software are detailed in the "Computational details" section and in the supplementary information (SI). Supplementary information is available. See DOI: **https://doi.org/10.1039/d5qm00921a**.

Acknowledgements

We acknowledge the CINECA award under the ISCRA initiative, for the availability of high-performance computing resources and support.

Notes and references

1 L. Han and M. Hong, Recent advances in the design and construction of helical coordination polymers, *Inorg. Chem. Commun.*, 2005, **8**, 406–419.

2 M. Lago-Silva, M. Fernández-Míguez, R. Rodríguez, E. Quiñoá and F. Freire, Stimuli-responsive synthetic helical polymers, *Chem. Soc. Rev.*, 2024, **53**, 793–852.

3 Y. Hu, S. J. Teat, W. Gong, Z. Zhou, Y. Jin, H. Chen, J. Wu, Y. Cui, T. Jiang, X. Cheng and W. Zhang, Single crystals of mechanically entwined helical covalent polymers, *Nat. Chem.*, 2021, **13**, 660–665.

4 J. Sun, L. Peng, Y. Liu and D. Wei, Highly Crystalline Helical Covalent Organic Frameworks, *Chem. Mater.*, 2024, **36**, 3666–3672.

5 E. Yashima, Synthesis and structure determination of helical polymers, *Polym. J.*, 2010, **42**, 3–16.

6 M. Xue, L. Zhang, X. Wang, Q. Dong, Z. Zhu, X. Wang, Q. Gu, F. Kang, X.-X. Li and Q. Zhang, A Metal-Free Helical Covalent Inorganic Polymer: Preparation, Crystal Structure and Optical Properties, *Angew. Chem., Int. Ed.*, 2024, **63**, e202315338.

7 E. Yashima, N. Ousaka, D. Taura, K. Shimomura, T. Ikai and K. Maeda, Supramolecular Helical Systems: Helical Assemblies of Small Molecules, Foldamers, and Polymers with Chiral Amplification and Their Functions, *Chem. Rev.*, 2016, **116**, 13752–13990.

8 E. Yashima, K. Maeda, H. Iida, Y. Furusho and K. Nagai, Helical Polymers: Synthesis, Structures, and Functions, *Chem. Rev.*, 2009, **109**, 6102–6211.

9 Z. Yi, H. Okuda, Y. Koyama, R. Seto, S. Uchida, H. Sogawa, S. Kuwata and T. Takata, Exact helical polymer synthesis by a two-point-covalent-linking protocol between C2-chiral spirobifluorene and C2- or Cs-symmetric anthraquinone monomers, *Chem. Commun.*, 2015, **51**, 10423–10426.

10 A. Santoro, J. Holub, M. A. Fik-Jaskółka, G. Vantomme and J.-M. Lehn, Dynamic Helicates Self-Assembly from Homo- and Heterotopic Dynamic Covalent Ligand Strands, *Chem. – Eur. J.*, 2020, **26**, 15664–15671.

11 J. Lee, Recent Progress in Synthesis of Conjugated Ladder Polymers, *Asian J. Org. Chem.*, 2023, **12**, e202300104.

12 J. Lee, A. J. Kalin, T. Yuan, M. Al-Hashimi and L. Fang, Fully conjugated ladder polymers, *Chem. Sci.*, 2017, **8**, 2503–2521.

13 A. J. Rothenberger, H. M. Bergman, H. Li, M. Qi, Y. Wang, Y. Liu and T. D. Tilley, Direct ladderization of cyclooctatetraene-containing, processable conjugated ladder polymers from annulated bis-zirconacyclopentadienes, *Chem. Sci.*, 2024, **15**, 20503–20508.

14 Y. C. Teo, H. W. H. Lai and Y. Xia, Synthesis of Ladder Polymers: Developments, Challenges, and Opportunities, *Chem. – Eur. J.*, 2017, **23**, 14101–14112.

15 X. Liu, Z. J. Weinert, M. Sharafi, C. Liao, J. Li and S. T. Schneebeli, Regulating Molecular Recognition with C-Shaped Strips Attained by Chirality-Assisted Synthesis, *Angew. Chem., Int. Ed.*, 2015, **54**, 12772–12776.

16 J. P. Campbell, M. Sharafi, K. E. Murphy, J. L. Bocanegra and S. T. Schneebeli, Precise molecular shape control of linear and branched strips with chirality-assisted synthesis, *Supramol. Chem.*, 2019, **31**, 565–574.

17 K. E. Murphy, K. T. McKay, M. Schenkelberg, M. Sharafi, O. Vestrheim, M. Ivancic, J. Li and S. T. Schneebeli, Helical Molecular Springs with Varying Spring Constants, *Angew. Chem., Int. Ed.*, 2022, **61**, e202209772.

18 G. Preda and D. Pasini, One-Handed Covalent Helical Ladder Polymers: The Dawn of a Tailorable Class of Chiral Functional Materials, *Angew. Chem., Int. Ed.*, 2024, **63**, e202407495.

19 T. Ikai, S. Miyoshi, K. Oki, R. Saha, Y. Hijikata and E. Yashima, Defect-Free Synthesis of a Fully π-Conjugated Helical Ladder Polymer and Resolution into a Pair of Enantiomeric Helical Ladders, *Angew. Chem., Int. Ed.*, 2023, **62**, e202301962.

20 Z. Pan and W. Zheng, Synthesis Amphiphilic One-Handed Helical Ladder Polymers with Circularly Polarized Luminescence, *Molecules*, 2025, **30**, 2606.

21 T. Ikai, A. Tanaka, T. Shiotani, K. Oki and E. Yashima, Secondary Structure Modulation of Triptycene-Based One-Handed Helical Ladder Polymers through π-Extension of Achiral Segments, *Org. Mater.*, 2023, **05**, 184–190.

22 J. S.-J. Yang and L. Fang, Conjugated ladder polymers: Advances from syntheses to applications, *Chem*, 2024, **10**, 1668–1724.

23 Z.-D. Yu, Y. Lu, J.-Y. Wang and J. Pei, Conformation Control of Conjugated Polymers, *Chem. – Eur. J.*, 2020, **26**, 16194–16205.

24 K. C. Chong, T. L. D. Tam, R. Tao, K. L. O. Chin, M. H. Chua and J. Xu, Conjugated Ladder Polymers: Unique Organic π-Conjugated Materials for Optoelectronics, Transistors, and Energy Harvesting and Storage, *Energy Mater Adv.*, 2025, **6**, 0134.

25 T. Ikai, N. Mishima, T. Matsumoto, S. Miyoshi, K. Oki and E. Yashima, 2,2′-Tethered Binaphthyl-Embedded One-Handed Helical Ladder Polymers: Impact of the Tether Length on Helical Geometry and Chiroptical Property, *Angew. Chem., Int. Ed.*, 2024, **63**, e202318712.

26 W. Zheng, T. Ikai and E. Yashima, Synthesis of Single-Handed Helical Spiro-Conjugated Ladder Polymers through Quantitative and Chemoselective Cyclizations, *Angew. Chem., Int. Ed.*, 2021, **60**, 11294–11299.

27 W. Zheng, K. Oki, R. Saha, Y. Hijikata, E. Yashima and T. Ikai, One-Handed Helical Tubular Ladder Polymers for Chromatographic Enantioseparation, *Angew. Chem., Int. Ed.*, 2023, **62**, e202218297.

28 T. Ikai, T. Matsumoto, S. Takeda, K. Oki and E. Yashima, Tunable Synthesis of One-Handed Helical Ladder Polymers with a Helical Cavity or Helical Grooves for Advanced Chiral Recognition, *Macromolecules*, 2025, **58**, 6943–6952.

29 M.-P. Van Den Eede, L. Van Gestel and G. Koeckelberghs, Expression of Chirality in Tailor-Made Conjugated Polymers, *Macromolecules*, 2018, **51**, 6602–6608.

30 B. Kiupel, C. Niederalt, M. Nieger, S. Grimme and F. Vögtle, "Geländer" Helical Molecules, *Angew. Chem., Int. Ed.*, 1998, **37**, 3031–3034.

31 A. Bedi and O. Gidron, The Consequences of Twisting Nanocarbons: Lessons from Tethered Twisted Acenes, *Acc. Chem. Res.*, 2019, **52**, 2482–2490.

32 J. Liu, X. Han, X. Wen, H. Yu, B. Li, M. Wang, M. Liu and G. Wu, Chiral ring-in-ring complexes with torsion-induced circularly polarized luminescence, *Chem. Sci.*, 2025, **16**, 7858–7863.

33 A. Giannetto, F. Nastasi, F. Puntoriero, G. Bella, S. Campagna and S. Lanza, Fast transport of HCl across a hydrophobic layer over macroscopic distances by using a Pt(ii) compound as the transporter: micro- and nanometric aggregates as effective transporters, *Dalton Trans.*, 2021, **50**, 1422–1433.

34 R. Ammenhäuser, J. M. Lupton and U. Scherf, Chain-Length Dependence of the Optical Activity of Helical Triptycene-Based π-Conjugated Ladder Polymers, *Adv. Optical Mater.*, 2024, **12**, 2301857.

35 T. Ikai, T. Yoshida, K.-I. Shinohara, T. Taniguchi, Y. Wada and T. M. Swager, Triptycene-Based Ladder Polymers with One-Handed Helical Geometry, *J. Am. Chem. Soc.*, 2019, **141**, 4696–4703.

36 B. Fernández, R. Rodríguez, A. Rizzo, E. Quiñoá, R. Riguera and F. Freire, Predicting the Helical Sense of Poly(phenylacetylene)s from their Electron Circular Dichroism Spectra, *Angew. Chem., Int. Ed.*, 2018, **57**, 3666–3670.

37 L. Ress, P. Malý, J. B. Landgraf, D. Lindorfer, M. Hofer, J. Selby, C. Lambert, T. Renger and T. Brixner, Time-resolved circular dichroism of excitonic systems: theory and experiment on an exemplary squaraine polymer, *Chem. Sci.*, 2023, **14**, 9328–9349.

38 Q. Yang, M. Fusè and J. Bloino, Theoretical Investigation of the Circularly Polarized Luminescence of a Chiral Boron Dipyrromethene (BODIPY) Dye, *Front. Chem.*, 2020, **8**, 801.

39 N. Chen and B. Yan, Recent Theoretical and Experimental Progress in Circularly Polarized Luminescence of Small Organic Molecules, *Molecules*, 2018, **23**, 3376.

40 G. Bella, G. Bruno and A. Santoro, Vibrationally resolved deep–red circularly polarised luminescence spectra of C70 derivative through Gaussian curvature analysis of ground and excited states, *J. Mol. Liq.*, 2023, **391**, 123268.

41 G. Bella, G. Bruno and A. Santoro, Ball Pivoting Algorithm and discrete gaussian curvature: A direct way to curved nanographene circularly polarized luminescence spectral simulation, *FlatChem*, 2023, **42**, 100567.

42 G. Bella, M. Milone, G. Bruno and A. Santoro, Triphasic circularly polarized luminescence switch quantum simulation of a topologically chiral catenane, *J. Mater. Chem. C*, 2024, **12**, 3005–3012.

43 R. Ammenhäuser, P. Klein, E. Schmid, S. Streicher, J. Vogelsang, C. W. Lehmann, J. M. Lupton, S. C. J. Meskers and U. Scherf, Circularly Polarized Light Probes Excited-State Delocalization in Rectangular Ladder-type Pentaphenyl Helices, *Angew. Chem., Int. Ed.*, 2023, **62**, e202211946.

44 M. Hatanaka, Size dependence of optical activities in helical polymers, *Chirality*, 2024, **36**, e23641.

45 É. Brémond, M. Savarese, N. Q. Su, Á. J. Pérez-Jiménez, X. Xu, J. C. Sancho-García and C. Adamo, Benchmarking Density Functionals on Structural Parameters of Small-/Medium-Sized Organic Molecules, *J. Chem. Theory Comput.*, 2016, **12**, 459–465.

46 G. Bella, A. Santoro, F. Nicolò, G. Bruno and M. Cordaro, Do Secondary Electrostatic Interactions Influence Multiple Dihydrogen Bonds? AA-DD Array on an Amine-Borane Aza-Coronand: Theoretical Studies and Synthesis, *Chem. Phys. Chem.*, 2021, **22**, 593–605.

47 G. Bella, M. Milone, G. Bruno and A. Santoro, Which DFT factors influence the accuracy of 1H, 13C and 195Pt NMR chemical shift predictions in organopolymetallic square-planar complexes? New scaling parameters for homo- and hetero-multimetallic compounds and their direct applications, *Phys. Chem. Chem. Phys.*, 2022, **24**, 26642–26658.

48 C. Zhao, R. Wu, S. Zhang and X. Hong, Benchmark Study of Density Functional Theory Methods in Geometry Optimization of Transition Metal–Dinitrogen Complexes, *J. Phys. Chem. A*, 2023, **127**, 6791–6803.

49 C. M. Cruz, S. Castro-Fernández, E. Maçôas, J. M. Cuerva and A. G. Campaña, Undecabenzo[7]superhelicene: A Helical Nanographene Ribbon as a Circularly Polarized Luminescence Emitter, *Angew. Chem., Int. Ed.*, 2018, **57**, 14782–14786.

50 C. M. Cruz, I. R. Márquez, S. Castro-Fernández, J. M. Cuerva, E. Maçôas and A. G. Campaña, A Triskelion-Shaped Saddle–Helix Hybrid Nanographene, *Angew. Chem., Int. Ed.*, 2019, **58**, 8068–8072.

51 M. A. Medel, R. Tapia, V. Blanco, D. Miguel, S. P. Morcillo and A. G. Campaña, Octagon-Embedded Carbohelicene as a Chiral Motif for Circularly Polarized Luminescence Emission of Saddle-Helix Nanographenes, *Angew. Chem., Int. Ed.*, 2021, **60**, 6094–6100.

52 S. Míguez-Lago, I. F. A. Mariz, M. A. Medel, J. M. Cuerva, E. Maçôas, C. M. Cruz and A. G. Campaña, Highly contorted superhelicene hits near-infrared circularly polarized luminescence, *Chem. Sci.*, 2022, **13**, 10267–10272.

53 Q. Xu, C. Wang, J. He, X. Li, Y. Wang, X. Chen, D. Sun and H. Jiang, Corannulene-based nanographene containing helical motifs, *Org. Chem. Front.*, 2021, **8**, 2970–2976.

54 Y.-J. Shen, N.-T. Yao, L.-N. Diao, Y. Yang, X.-L. Chen and H.-Y. Gong, A π-Extended Pentadecabenzo[9]Helicene, *Angew. Chem., Int. Ed.*, 2023, **62**, e202300840.

55 G. Bella, G. Bruno and A. Santoro, Circular dichroism simulations of chiral buckybowls by means curvature analyses, *FlatChem*, 2023, **40**, 100509.

56 B. C. Ferrari and C. J. Bennett, A Comparison of Medium-Sized Basis Sets for the Prediction of Geometries, Vibrational Frequencies, Infrared Intensities and Raman Activities for Water, *J. Phys.: Conf. Ser.*, 2019, **1290**, 012013.

57 G. Bella, A. Santoro, M. Cordaro, F. Nicolò and G. Bruno, Isoxazolone Reactivity Explained by Computed Electronic Structure Analysis, *Chin. J. Chem.*, 2020, **38**, 163–168.

58 K. Żamojć, D. Jacewicz and L. Chmurzyński, Quenching of Fluorescence of Polycyclic Aromatic Hydrocarbons by 4-OH-TEMPO, *Anal. Lett.*, 2013, **46**, 349–355.

59 Z. Kausar, A. Mansha and S. Asim, Effect of Chloride, Sulfate, and Ferrate Salts on Electronic Energy Levels of Anthracene Proving it a Potential Candidate as an ON and ON–OFF UV–Vis Sensor, *J. Fluoresc.*, 2024, **34**, 1365–1378.

60 Y. Nagata and T. Mori, Irreverent Nature of Dissymmetry Factor and Quantum Yield in Circularly Polarized Luminescence of Small Organic Molecules, *Front. Chem.*, 2020, **8**, 448.

61 M. J. Frisch, G. W. Trucks, H. B. Schlegel, G. E. Scuseria, M. A. Robb, J. R. Cheeseman, G. Scalmani, V. Barone, G. A. Petersson, H. Nakatsuji, X. Li, M. Caricato, A. V. Marenich, J. Bloino, B. G. Janesko, R. Gomperts, B. Mennucci, H. P. Hratchian, J. V. Ortiz, A. F. Izmaylov, J. L. Sonnenberg, Williams, F. Ding, F. Lipparini, F. Egidi, J. Goings, B. Peng, A. Petrone, T. Henderson, D. Ranasinghe, V. G. Zakrzewski, J. Gao, N. Rega, G. Zheng, W. Liang, M. Hada, M. Ehara, K. Toyota, R. Fukuda, J. Hasegawa, M. Ishida, T. Nakajima, Y. Honda, O. Kitao, H. Nakai, T. Vreven, K. Throssell, J. A. Montgomery Jr., J. E. Peralta, F. Ogliaro, M. J. Bearpark, J. J. Heyd, E. N. Brothers, K. N. Kudin, V. N. Staroverov, T. A. Keith, R. Kobayashi, J. Normand, K. Raghavachari, A. P. Rendell, J. C. Burant, S. S. Iyengar, J. Tomasi, M. Cossi, J. M. Millam, M. Klene, C. Adamo, R. Cammi, J. W. Ochterski, R. L. Martin, K. Morokuma, O. Farkas, J. B. Foresman and D. J. Fox, *Gaussian 16 Rev. C.01*, Wallingford CT, 2016.

62 W. Humphrey, A. Dalke and K. Schulten, VMD: Visual molecular dynamics, *J. Mol. Graphics*, 1996, **14**, 33–38.

63 T. Lu and F. Chen, Multiwfn: A multifunctional wavefunction analyzer, *J. Comput. Chem.*, 2012, **33**, 580–592.

64 J. B. Maglic and R. Lavendomme, MoloVol: an easy-to-use program for analyzing cavities, volumes and surface areas of chemical structures, *J. Appl. Cryst.*, 2022, **55**, 1033–1044.